BROOKHAVEN NATIONAL LABORATORY

BNL-107329-2014-JA

Si+-implanted Si-wire waveguide photodetectors for the mid-infrared

Brian Souhan[1], Richard R. Grote[1], Christine P. Chen[2], Hsu-Cheng Huang[1], Jeffrey B. Driscoll[1], Ming Lu[3], Aaron Stein[3], Hassaram Bakhru[4], Keren Bergman[2], William M. J. Green5, and Richard M. Osgood, Jr.[1]

[1]Microelectronics Sciences Laboratories, Columbia University, 500 W. 120th Street, New York New York, NY 10027, USA
[2]Department of Electrical Engineering, Columbia University, 500 W. 120th Street, New York, NY 10027, USA
[3]Center for Functional Nanomaterials, Brookhaven National Laboratory, PO Box 5000, Upton, NY 11973, USA
[4]College of Nanoscale Science and Engineering, State University of New York at Albany, Albany, NY 12222, USA
[5]IBM T. J. Watson Research Center, 1101 Kitchawan Rd., Yorktown Heights, NY 10598, USA

Submitted to Optics Express

November 2014

Center for Functional Nanomaterials

Brookhaven National Laboratory

U.S. Department of Energy
Office of Science, Basic Energy Sciences

DISCLAIMER

Si^+-implanted Si-wire waveguide photodetectors for the mid-infrared

Brian Souhan,[1*] Richard R. Grote,[1] Christine P. Chen,[2] Hsu-Cheng Huang, [1] Jeffrey B. Driscoll,[1] Ming Lu,[3] Aaron Stein,[3] Hassaram Bakhru,[4] Keren Bergman[2], William M. J. Green[5], and Richard M. Osgood, Jr.[1]

[1]*Microelectronics Sciences Laboratories, Columbia University, 500 W. 120th Street, New York New York, NY 10027, USA*

[2]*Department of Electrical Engineering, Columbia University, 500 W. 120th Street, New York, NY 10027, USA*

[3]*Center for Functional Nanomaterials, Brookhaven National Laboratory, PO Box 5000, Upton, NY 11973, USA*

[4]*College of Nanoscale Science and Engineering, State University of New York at Albany, Albany, NY 12222, USA*

[5]*IBM T. J. Watson Research Center, 1101 Kitchawan Rd., Yorktown Heights, NY 10598, USA*

[*]*brian.souhan@gmail.com*

Abstract: CMOS-compatible Si^+-implanted Si-waveguide *p-i-n* photodetectors operating at room temperature and at mid-infrared wavelengths from 2.2 to 2.3 μm are demonstrated. Responsivities of 9.9 ± 2.0 mA/W are measured at a 5 V reverse bias with an estimated internal quantum efficiency of 2.7 – 4.5%. The dark current is found to vary from a few microamps down to less than a nanoamp after a post-implantation annealing of 350°C. The measured photocurrent dependence on input power shows a linear correspondence over more than three decades, and the frequency response of a 250μm-length *p-i-n* device is measured to be ~1.7 GHz for a wavelength of λ = 2.2 μm, thus potentially opening up new communication bands for photonic integrated circuits.

OCIS codes: (040.6040) Silicon; (040.5160) Photodetectors; (130.3120) Integrated optics devices.

References and links

1. R. Soref, "Mid-infrared photonics in silicon and germanium," Nature Photonics **4**, 495-497 (2010).
2. D. J. Thomson, L. Shen, J. J. Ackert, E. Huante-Ceron, A. P. Knights, M. Nedeljkovic, A. C. Peacock, and G. Z. Mashanovich, "Optical detection and modulation at 2μm-2.5μm in silicon," Opt. Express **22**, 10825-10830 (2014).
3. B. Souhan, C. P. Chen, R. R. Grote, J. B. Driscoll, N. Ophir, K. Bergman, and R. M. Osgood, "Error-Free Operation of an All-Silicon Waveguide Photodiode at 1.9μm," IEEE Photon. Technol. Lett. **25**, 2031-2034 (2013).
4. N. Ophir, R. K. W. Lau, M. Ménard, R. Salem, K. Padmaraju, Y. Okawachi, M. Lipson, A. L. Gaeta, and K. Bergman, "First Demonstration of a 10-Gb/s RZ End-to-End Four-Wave-Mixing Based Link at 1884 nm Using Silicon Nanowaveguides," IEEE Photon. Technol. Lett., **24**, 276-278 (2012).
5. G. Roelkens *et al.*, "Silicon-based heterogeneous photonic integrated circuits for the mid-infrared," Opt. Mater. Express **3**, 1523-1536 (2013).
6. P. T. Lin, V. Singh, J. Wang, H. Lin, J. Hu, K. Richardson, J. D. Musgraves, I. Luzinov, J. Hensley, L. C. Kimerling, and A. Agarwal, "Si-CMOS compatible materials and devices for mid-IR microphotonics," Opt. Mater. Express **3**, 1474-1487 (2013).
7. R. R. Grote, B. Souhan, N. Ophir, J. B. Driscoll, K. Bergman, H. Bahru, W. M. J. Green, and R. M. Osgood, "Zn^+ Implanted Silicon waveguide Photodiodes for On-Chip Mid-Infrared Detection," in *Conference on Lasers and Electro-Optics*, Technical Digests (online) (Optical Society of America, 2014), paper Stu3G.1
8. R. R. Grote, B. Souhan, N. Ophir, J. B. Driscoll, K. Bergman, H. Bahru, W. M. J. Green, and R. M. Osgood, "Extrinsic Photodiodes for Integrated Mid-Infrared Silicon Photonics," arXiv:1406.6420
9. M. A. Van Camp, S. Assefa, D. M. Gill, T. Barwicz, S. M. Shank, Y. A. Vlasov, W. M. Green, "Demonstration of Electrooptic Modulation at 2165nm Using a Silicon Mach-Zehnder Interferometer," Optics Express **20**(27), 28009-28016 (2012).

10. N. V. Wheeler, A. M. Heidt, N. K. Baddela, E. N. Fokoua, J. R. Hayes, S. R. Sandoghchi, F. Poletti, M. N. Petrovich, and D. J. Richardson, "Low-loss and low-bend-sensitivity mid-infrared guidance in a hollow-core-photonic-bandgap fiber," Optics Letters 39(2), 295-298 (2014).
11. N. Sclar, " Properties of doped silicon and germanium infrared detectors," Progress in Quantum Electronics **9**(3), 149-257 (1984).
12. R. R. Grote, K. Padmaraju, B. Souhan, J. B. Driscoll, K. Bergman, and R. M. Osgood, "10 Gb/s Error-Free Operation of All-Silicon Ion-Implanted-Waveguide Photodiodes at 1.55μm," IEEE Photon. Technol. Lett. **25**, 67-70 (2013).
13. M. W. Geis, S. J. Spector, M. E. Grein, R. T. Schulein, J. U. Yoon, D. M. Lennon, S. Deneault, F. Gan, F. X. Kaertner, and T. M. Lyszczarz, "CMOS-Compatible All-Si High-Speed Waveguide Photodiodes With High Responsivity in Near-Infrared Communication Band," IEEE Photon. Technol. Lett. **19**, 152-154 (2007).
14. B. Souhan, R. R. Grote, J. B. Driscoll, M. Lu, A. Stein, H. Bakhru, and R. M. Osgood, "Metal-semiconductor-metal ion-implanted Si waveguide photodetectors for C-band operation," Opt. Express **22**, 9150-9158 (2014)
15. M. W. Geis, S. J. Spector, M. E. Grein, R. T. Schulein, J. U. Yoon, D. M. Lennon, C. M. Wynn, S. T. Palmacci, F. Gan, F. X. Kärtner, and T. M. Lyszczarz, "All silicon infrared photodiodes: photo response and effects of processing temperature," Opt. Express **15**, 16886-16895 (2007).
16. M. W. Geis, S. J. Spector, M. E. Grein, J. U. Yoon, D. M. Lennon, and T. M. Lyszczarz, "Silicon waveguide infrared photodiodes with >35GHz bandwidth and phototransistors with 50 AW^{-1} response," Opt. Express **17**, 5193-5204 (2009).
17. B. Souhan, R. Grote, J. Driscoll, H. Bakhru, R. M. Osgood, "CMOS Compatible Argon-Ion-Implanted C-Band Silicon waveguide Photodetector," in *Conference on Lasers and Electro-Optics*, Technical Digest (online) (Optical Society of America, 2013), paper CTh3L.3.
18. J. D. B. Bradley, P. E. Jessop, and A. P. Knights, "Silicon waveguide-integrated optical power monitor with enhanced sensitivity at 1550 nm," Appl. Phys. Lett. **86**, 241103 (2005).
19. R. Dey, J. Doylend, J. Ackert, A. Evans, P. Jessop, A. Knights, "Demonstration of a wavelength monitor comprised of racetrack-ring resonantors with defect mediated photodiodes operating in the C-band," Opt. Express **21**, 23450-23458 (2013).
20. K. Padmaraju, J. Chan, L. Chen, M. Lipson, and K. Bergman, "Thermal stabilization of a microring modulator using feedback control," Opt. Express **20**, 27999-28008 (2012).
21. S. Park, K. Yamada, T. Tsuchizawa, T. Watanabe, H. Nishi, H. Shinojima, and S. Itabashi, "All-silicon and in-line integration of variable optical attenuators and photodetectors based on submicrometer rib waveguides," Opt. Express **18**, 15303-15310 (2010).
22. J. F. Ziegler, M.D. Ziegler, and J.P. Biersack, "SRIM – The Stopping and Range of Ions in Matter (2010)", Nucl. Inst. Methods B268, 1818-1823 (2010).
23. M. Casalino, L. Sirleto, L. Moretti, M. Gioffrè, and I. Rendina, "Low dark current silicon-on-insulator waveguide metal-semiconductor-metal photodetector based on internal photoemisions at 1550nm," J. Appl. Phys. **114**, 153103 (2013).
24. H. Y. Fan and A. K. Ramdas, "Infrared Absorption and Photoconductivity in Irradiated Silicon," J. Appl. Phys. **30**, 1127-1134 (1959).
25. J. Michel, S. J. Koester, J. Liu, X. Wang, M. W. Geis, S. J. Spector, M. E. Grein, J. U. Yoon, T. M. Lyszczarz, and N. Feng, *Handbook of Si Photonics*, (Taylor and Francis, 2013), Chap. 10.
26. J. J. Ackert, A. S. Karar, D. J. Paez, P. E. Jessop, J. C. Cartledge, and A. P. Knights, "10 Gbs silicon waveguide-integrated infrared avalanche photodiode," Opt. Express **21**, 19530-19537 (2013).
27. EOSpace Electro-Optic Modulators, Switches, and Custom Integrated Optical Circuits, www.eospace.com.
28. R. Siemieniec, H.-J. Schulze, F.-J. Niedernostheide, W. Südkamp, and J. Lutz, "Compensation and doping effects in heavily helium-radiated silicon for power device applications," Microelectronics Journal **37**, 204-212 (2006).

---

1. Introduction

Recently, the inherent transparency of integrated Si photonic structures to both single- and two-photon absorption at mid-infrared (IR) wavelengths ($\lambda = 2 - 5$ μm) has begun to be utilized, giving rise to new applications in chemical and biological sensing, free-space communications, and spectroscopy [1]. Use of this wavelength region (particularly at the shorter wavelengths) also holds promise for yielding new spectral bands for optical communication systems [2]. The introduction of thulium-doped fiber amplifiers designed to operate in the 2 μm range has been shown to facilitate the use of additional communication

bands beyond 1.3 μm and 1.55 μm [3, 4], while the investigation of several materials and components is also underway for use in the 2 μm – 3 μm range [2,5-9], including hollow-core fiber technology that has recently been shown to be applicable for transmission systems at even longer wavelengths [10].

Currently, the majority of mid-IR photonic systems have been composed of discrete components rather than a more desired truly integrated system [1]. One vital component for a complete integrated system is an integrated photodetector (PD). Several researchers have demonstrated heterogeneously integrated detectors for the mid-IR made from GeSn [5], GaSb [5], PbTe colloidal quantum dots [5] and PbTe photoconductors using chalcogenide glass waveguides [6]. While many of these devices exhibit high responsivities, the heterogeneous integration of binary materials incorporated into a Si photonic system requires additional processing beyond traditional Complimentary-Metal-Oxide-Semiconductor (CMOS) processes.

Alternatively, ion implantation is well known to create optically active sub-bandgap trap-states in Si due to a variety of lattice defects, including divacancies, vacancy-oxygen complexes, and Si interstitial clusters; note that this process is distinct from substitional doping used pervasively in doping for Si electronics which can also be used for mid-infrared detection [11]. The formation of these different defects depends on the annealing temperature and implant species, and this approach has been utilized extensively to make on-chip Si waveguide (SiWG) PDs for 1.55μm [12-17]. These ion-implanted SiWG PDs have been demonstrated in numerous systems including data interconnects [3,12], power monitors [17], wavelength monitors [18], thermal device stabilization controllers [19], and variable optical attenuators [20]. These devices are known to exhibit high frequency response, low dark current, and responsivities greater than 1 A/W, making them ideal for numerous applications [12-17].

Only recently have ion-implanted PDs been explored for the mid-IR band with the demonstration of both boron and zinc implanted SiWG *p-i-n* PDs [2,7,8]. Responsivities of 1.7 mA/W was seen for the boron implanted PDs (reverse bias unknown) [2], and as high as 87 mA/W (20V reverse bias) [7,8] was seen for the zinc implanted PDs at a wavelength of 2.2 μm. Furthermore, PD operation is expected out to 3.3 μm based on experimental data from deuterium implanted Si for PDs [24].

In this paper, *p-i-n* PDs based on a Si rib-waveguide geometry with a 520 nm × 220 nm channel section and 50 nm 'wings' as shown in Fig. 1 are used to characterize CMOS-compatible Si^+ ion-implanted SiWGs at $\lambda = 2.2 - 2.3$ μm for different annealing temperatures and implantation conditions. The Si^+-implanted devices measured in this paper exhibited responsivities (at $\lambda = 2.2$ μm) within the range from 4.2 – 9.9 mA/W after annealing at 200˚C, and 2.8 – 7.2 mA/W after annealing at 350˚C; both at a 5 V reverse bias. Further, internal quantum efficiencies (IQE) ranging from 2.7% − 4.5% for a 5 V reverse bias are calculated. The detector's frequency response is measured to be 1.7 GHz, limited by an un-optimized RC time constant. The dark current is found to be as low as 8.5 pA at 0 V to 3.55 nA at 10V for a 250 μm length device annealed at 350˚C. The demonstrated device characteristics, combined with the relatively simple additional processing beyond that which is required for fabricating conventional passive Si waveguides, illustrate the potential benefits of using Si^+ implanted detectors in various long-wavelength integrated-Si-photonic applications.

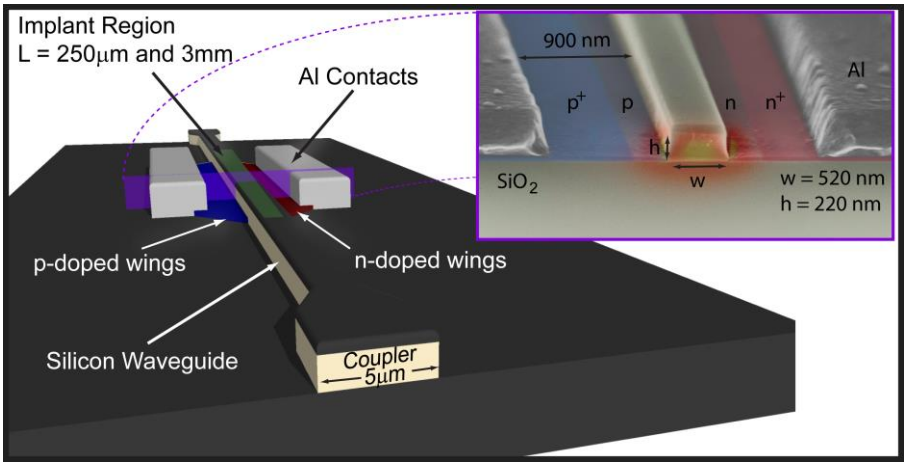

Fig. 1. Schematic model of the characterized device. The inset shows a false color SEM cross-section of a *p-i-n* device with the calculated mode at 2.2 μm incident on the waveguide.

2. Device Design and Fabrication

The base *p-i-n* devices into which Si^+ ions were implanted were fabricated at MIT Lincoln Labs, as described in [13]. The Si waveguide channel was 520 × 220 nm with 50 nm high 'wings' for the electrical connection to the contacts. The contacts consisted of 300 nm Al on top of a 10 nm W adhesion layer. Coupling onto and off of the chip was accomplished through 5 μm wide fan out tapers, through which input/output facets were cleaved. Due to the low absorption coefficient of the devices, not all of the optical power was absorbed, facilitating transmission as well as photocurrent measurements. The 'wings' were doped with concentrations of 10^{19} cm^{-3} and 10^{18} cm^{-3} for the p^+ (boron), n^+ (phosphorus) and *p*, *n* regions respectively. Additional rib and channel waveguides for basic absorption-coefficient measurements were fabricated as described in [14] with channel dimensions for both of 650 × 220 nm and 73nm 'wings' for the rib waveguides. These waveguides were not made into PDs, only undergoing the Si^+ ion-implantation process, with no boron/phosphorus doping or metal contact deposition, in order to minimize parasitic losses. Both sets of devices were subsequently masked to open windows ranging from 250 μm to 3 mm in length and implanted with Si^+ ions at the Ion Beam Laboratory, at the State University at Albany. The implantation dose was 1×10^{13} cm^{-2} Si^+ with an implantation energy of 190 keV and beam-current densities of ≈ 10 nA/cm^2 and ≈ 15 nA/cm^2. The beam diameter was between 3-4 mm and scanned over a 2 in radius circle, in which the chips were placed. Contact photolithography was used to create an ion implantation mask using Shipley 1811, with a 250 μm – 3mm long by 8 μm wide window centered over the channel section of the SiWG. The implantation energy and dose were based on prior reports of ion-induced defects [13-16] and Stopping Range of Ions in Matter (SRIM) calculations [22] and were chosen such that the defect concentration overlapped maximally with the fundamental quasi-TE waveguide mode (illustrated in the inset of Fig. 1). After implantation, the devices were annealed in atmosphere at 150°C for 10 minutes and the PD response was characterized. Subsequently, the same PD devices were annealed at an elevated temperature of 200°C for 10 minutes, and then characterized again. This process was repeated with annealing temperatures increasing in increments of 50°C up to a final temperature of 350°C. This final annealing temperature was constrained by reflow of the metal contacts. For photocurrent measurements, three *p-i-n* devices were used with the parameters given in Table 1 below.

Table 1. Implantation parameters of the three tested PDs.

	Implant-Window Length	Implant Energy	Dose	Beam Current Density
PD 1	3 mm	190 keV	10^{13} cm^{-2}	15 nA/cm^2
PD 2	250 µm	190 keV	10^{13} cm^{-2}	10 nA/cm^2
PD 3	3 mm	190 keV	10^{13} cm^{-2}	10 nA/cm^2

3. Results and Discussion

3.1 Photocurrent and Linearity

Device measurements were taken utilizing a tunable external-cavity Cr^{2+}:ZnSe laser, operating across a wavelength range from λ = 2.2 to 2.4 µm. A fiber collimator was used to couple light into a standard single-mode fiber (SMF), which in turn was connected to a lens tapered fiber (LTF) for coupling light onto the chip. Optical launch power was measured at the connection of the SMF and LTF with an infrared optical spectrum analyzer (OSA). An additional LTF was used to couple the output optical power from the chip. Optical output power was measured utilizing an OSA at the end of a 1 m section of SMF. System losses were characterized utilizing several un-implanted straight waveguides on each chip following the procedures described in Appendix A. The total input optical power losses prior (including LTF loss, coupling loss, and waveguide loss) to the PD were 9.2 – 11.8 dB for PD 1 and 7.9 – 9.7 dB for PDs 2 and 3.

Figure 2(a) shows the measured photocurrent for PD 1 (annealed to 200˚C) at λ = 2.2 µm for an incident power (power incident at the beginning of the implantation region) of 3.0 ± 1.2 mW, and the photocurrent for PD 3 (annealed to 350˚C) at λ = 2.2 µm with an incident power of 2.7 ± 0.6 mW. The photocurrent measurements exhibited diode-like characteristics, verifying the results were not from photoconduction. Although the photocurrent is slightly lower for PD 3 after the higher annealing temperature, the corresponding dark current was over an order of magnitude lower, thus reducing noise equivalent power, improving detector performance, and decreasing overall power consumption [23].

To measure device linearity, the launch power was varied via the adjustment of focusing of the free-space-to-SMF connection. The results for PD 1 (200˚C annealing) and PD 3 (350˚C) are shown in Fig. 2(b) for λ = 2.2 µm. It is clear from the unity slope of the graph that the detectors are linear over ≈ 4 decades, from an incident power of ≈ 0.5 µW to ≈ 3.7 mW. Linearity of photocurrent generation with launch power was observed for all PDs, annealed at all temperatures >150˚C, thus verifying that the defect-mediated absorption is a single-photon process.

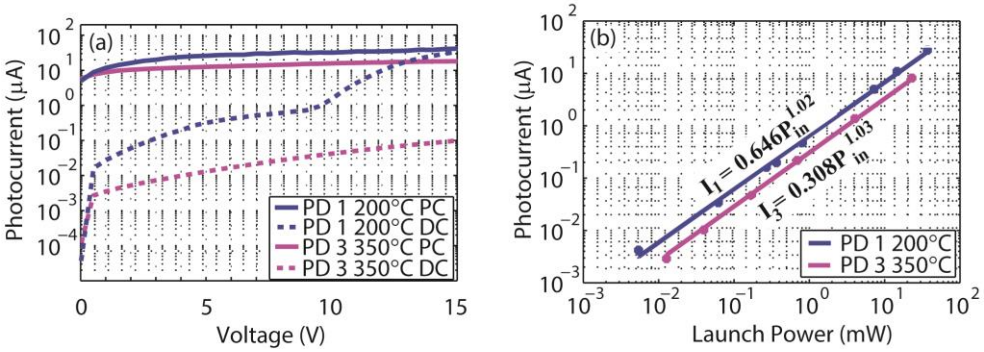

Fig. 2. (a) Photocurrent (PC) and dark current (DC) plot for PD 1, annealed at 200˚C with 3.0 ± 1.2 mW incident power and PD 3 annealed at 350˚C with 2.7 ± 0.6 mW incident power. (b) Photocurrent *versus* launch power showing linearity for PD 1 and PD 3 under the same conditions. All measurements were taken at λ = 2.2 μm.

3.2 Responsivity

Responsivity was determined by subtracting the photodiode dark current from the light current with illumination and dividing by the incident power in the detector, $\Re = (I_{light} - I_{dark}) / P_{inc}$. Figure 3(a) shows the measured responsivity at 5 V versus annealing temperature for the three devices. The responsivity curves for all devices show local maxima for 200˚C annealing. As the annealing temperature increased beyond 250˚C, again for all devices, responsivity resumed increasing until the maximum anneal temperature of 350˚C was reached. The peak at 200˚C is believed due to the formation and subsequent annealing of the divacancy defect, as has previously been observed in ion-implanted PDs in this temperature range [13,15,16,24], and is known to anneal out at temperatures near or above 200˚C [13,15,16,24]. The cause of the increase in responsivity due to additional annealing above 250˚C is not fully established, however this increase is tentatively attributed, in part, to non-optically active carrier recombination centers annealing out, increasing carrier lifetime and resulting in decreased gain in photocurrent with increased bias, as seen in Fig. 2(a). However, as the divacancy defect is known to anneal out in this temperature range, it is unclear whether the divacancy is still the primary absorption state or if other unknown defect states are contributing. Additionally, although all three PDs exhibited the same general characteristics with annealing, a significant difference in responsivity and dark current was seen between the two different implantation currents, suggesting that implantation current is a critical parameter in determining device characteristics; this point may also be reflected in the fact that significant variations have been seen in these devices [25].

Figure 3(b) shows the responsivity as a function of bias voltage for PD 1 after annealing at 200˚C and PD 3 after annealing at 350˚C, along with the responsivity for an un-implanted device. Photodiode 1 achieved the maximum responsivity of all the devices after the 200˚C anneal, with a responsivity of 9.9 mA/W at λ = 2.2 μm and a 5 V reverse bias. Increasing the bias to 15 V approximately doubled the responsivity at the cost of increasing the dark current by nearly two orders of magnitude. Photodiode 2 and PD 3, implanted at a lower implantation current showed less dependence on anneal temperature, an order of magnitude less dark current, and exhibited maximum responsivities of 7.2 mA/W and 5.1 mA/W after the 350˚C anneal with λ of 2.2 μm and a reverse bias of 5V.

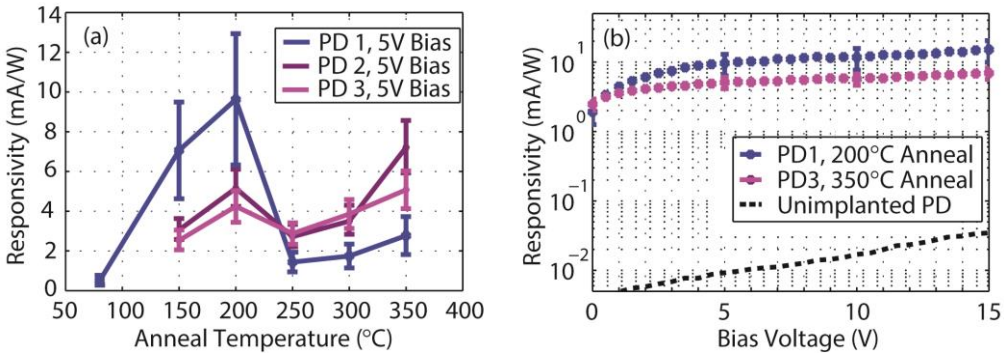

Fig. 3. (a) Responsivity *versus* annealing temperature for the three devices taken at λ = 2.2 μm. The peak at 200°C is consistent with the formation and subsequent annealing of the divacancy defect. Error bars are based on the measured deviation in measured loss prior to the detector. (b) Responsivity *versus* bias voltage for PD 1 and PD 3 taken at λ = 2.2 μm under different annealing conditions.

3.3 Absorption and Internal Quantum Efficiency

Implantation-induced modal absorption coefficients for the waveguides were found using the cutback method on sets of three different-length ion-implanted rib and channel waveguides. The channel waveguides were implanted under the same conditions as PD 2 and PD 3 (beam current density ≈ 10 nA/cm^2), while the rib waveguides were implanted under the same conditions as PD 1 (beam current density ≈ 15 nA/cm^2). The material absorption coefficients as shown in Fig. 4(a) were determined from the measured modal absorption coefficients by doing a parameter scan with a finite-element-method solver. The material absorption coefficients, $\alpha_{material}$, were calculated and plotted in order to compare measurements from different waveguide geometries and bulk data from the literature.

Unlike the variation in the measured responsivities for waveguides annealed at 200˚C for different implantation conditions, our measured material absorption coefficients were found to be in good agreement. Further, the bulk absorption coefficients at 200˚C of 58 - 73 dB/cm at λ = 2.2 μm were well matched to the ~ 60 dB/cm value reported for bulk Si with deuterium implantation at λ = 2.214 μm [24]. In our experiments, a significant decrease was seen in the absorption coefficient with annealing to 350 ˚C, suggesting annealing out of defects.

Device IQE was estimated based on the measured modal absorption coefficients, the measured responsivities, and the PD parasitic loss found by measuring transmission through un-implanted *p-i-n* PDs. Since the *p-i-n* PDs were designed for operation at 1.55 μm, the parasitic losses were significant, ranging from 249 dB/cm to 826 dB/cm for λ = 2.2 to 2.3 μm [7,8].

Responsivity in A/W can be expressed in terms of an external quantum efficiency η_e as: $\Re = \eta_e \cdot \lambda / 1.24$, with λ in micrometers. In the absence of reflection, the external quantum efficiency for a waveguide PD, η_e, is:

$$\eta_i \cdot \alpha_{modal} / (\alpha_{modal} + \alpha_{par}) \cdot (1 - e^{-(\alpha_{modal} + \alpha_{par}) \cdot L}), \quad (1)$$

where η_i is defined as the percentage of electron-hole pairs absorbed by photoactive defects that contribute to current (IQE), and α is the absorption coefficient, either modal or parasitic as annotated. The ratio $\alpha_{modal} / (\alpha_{modal} + \alpha_{par})$ determines the ratio of photons absorbed *versus* loss to parasitic losses and *L* is the length of the device. Using these equations, η_i was

calculated to be between 2.7 ± 0.9% to 4.5 ± 1.1% for a bias voltage of 5 V at λ = 2.2 µm. The large error for the PD 1 at λ = 2.225 µm was a result of the large difference in the measured absorption coefficient at that wavelength and due to limited data. Figure 4(b) shows the IQE versus wavelength, with the general trend of decreasing IQE with increasing wavelength. The IQE of PD 2 after annealing at 350˚C appears higher than that of PD 1 despite the lower responsivity at λ = 2.2 µm; note however, that the difference was within the measurement error.

As mentioned earlier, the *p-i-n* devices used for measurements were initially designed for operation at λ = 1.55 µm. With the doping of the wings in close proximity to the waveguide, and the small contact separation, the parasitic losses of the devices were extremely high. Redesigning the device such that the contacts and doped wing regions are spaced further from the waveguide, such as carried out in [26], will enable the parasitic losses to be significantly reduced. If parasitic losses are reduced to ~ 7 dB/cm as measured in [13,15,16] for λ = 1.55 µm, responsivities ≈ 60 – 70 mA/W are possible based on the measured absorption coefficients and calculated IQEs. Avalanche multiplication, as demonstrated in [26] for λ = 1.55 µm operation, may lead to even greater responsivities.

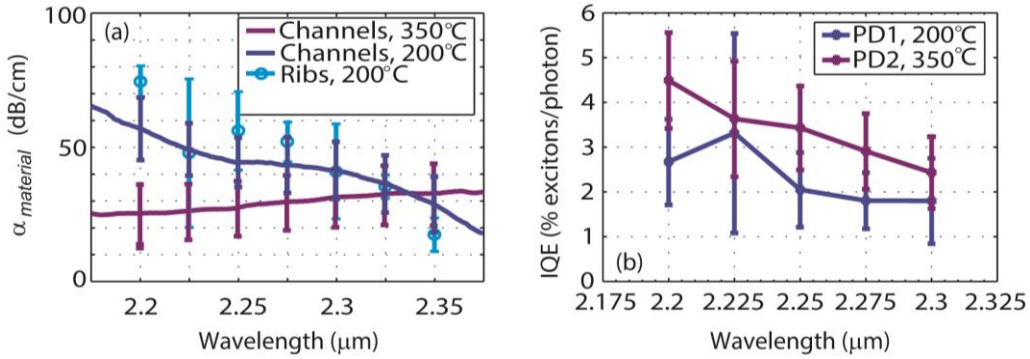

Fig. 4. (a) Measured absorption coefficients for implanted channel and rib waveguides. Error bars for the channel waveguides ranged from a minimum error of ≈ 11 dB/cm occurring at 2.35 µm to ≈ 14 dB/cm occurring at 2.2 µm, while varied significantly for the rib guides, ranging from 6 to 27 dB/cm. Due to lower losses of the channel guides, the laser amplified spontaneous emission was used for measurements resulting in a continuous spectral function. (b) Calculated IQE for PD 1 after annealing at 200˚C anneal and PD 2 after annealing at 350˚C.

3.4 Frequency Response

A lightwave component analyzer (LCA) in conjunction with an EOSpace long-λ (2-µm) $LiNbO_3$ modulator [27] was used to determine the frequency response of PD 2 and PD 3 after annealing each to 200˚C. The normalized responsivity was plotted based on a 50 Ω load and the results shown below are for an un-optimized device, as Si^+ implantation in the 'wings' region likely impacted both resistance and capacitance from the values reported in [13,15,16] as the divacancy defect is known to act as compensation doping [28], however further experimentation is needed to verify this. A bias voltage of 20 V was used along with λ = 2.2 µm for PD 2, while a bias voltage of 25V was used for PD 3 due to the slightly lower responsivity. The increase in frequency response seen for a decrease in length suggested the devices are RC limited, which was also seen for similar devices at shorter wavelengths [3,13,16]. Given the waveguide dimensions, the electric field with a 20 V bias was expected to be sufficiently high for the carriers to reach saturation velocity, even with the reduction in carrier mobility as reported in [14] for ion-implantation. With device optimization, including limiting implantation overlap with the 'wings' of the detector, frequency responses of greater than 10 GHz are expected, as was demonstrated in [13,16] for similar but shorter-wavelength SiWG photodiodes.

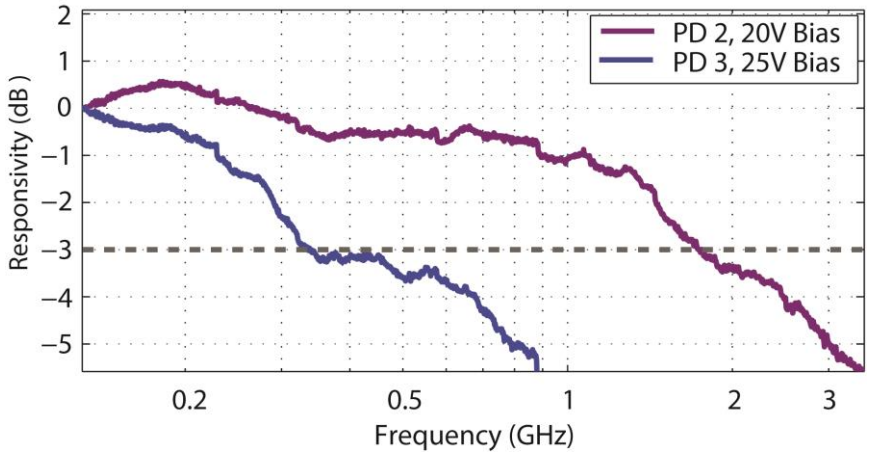

Fig. 5. Frequency response for PD 2 (250 µm) and PD 3 (3 mm) at λ of 2.2 µm after the 200˚C anneal. The frequency response indicates the devices are limited by RC. The slight oscillatory modulation on the response curves was a result of reflections in measurement apparatus and was seen in other detector measurements.

4. Conclusion

CMOS compatible integrated Si^+-implanted SiWG photodetectors have been demonstrated and characterized for use in the mid-IR. These devices have measured maximum responsivities of ~ 10 mA/W for a 5 V reverse bias, higher than previously reported for other ion-implanted waveguide detectors at this wavelength [2,7,8], and responsivities as high as 3 mA/W for no applied bias with dark currents of only 10's of picoamps. The detector frequency response was measured to bet 1.7 GHz, with elimination of implantation in the device wings expected to lead to a factor of 5-10 increase in frequency responses. Significant increases in responsivity ≈ 60 - 70 mA/W are expected based on the calculated IQE of 2.7 – 4.5%. Although this responsivity is significantly lower than that reported for heterogeneously integrated detectors based on binary materials, their simple fabrication, low dark current, CMOS compatibility, and high speed operation makes these devices desirable for a variety of applications in integrated Si photonic systems.

5. Appendix A

To determine the total loss prior to the detector, the cutback method was used on waveguides consisting of identical 5 µm × 220 nm fan-out coupling taper sections and un-implanted straight waveguide sections. Multiple measurements were done on multiple devices to obtain an average total loss and standard deviation for each chip. Loss measurements were initially done in dB and then converted to the appropriate ratio of P_{out}/P_{in} prior to averaging and finding the standard deviation. The conversion to P_{out}/P_{in} was done based on the assumption of normally distributed error *versus* a log-normal distribution. The results gave a total loss prior to the PD, including LTF loss, coupling loss, and waveguide loss.

Responsivity was determined by utilizing the average loss to calculate incident power with the corresponding error bars based on the standard deviation of the input power as determined from the above measurements.

$$\Re = I_{photo} / (P_{inc} \pm \Delta P_{inc}) \tag{2}$$

For the IQE measurements, the propagation of error formula both for multiplication of two standard variables (f = A·B) and for division of two standard variables (f = A/B) assuming negligible covariance is

$$\sigma_f \approx |f| \sqrt{\left(\frac{\sigma_A}{A}\right)^2 + \left(\frac{\sigma_B}{B}\right)^2} \,. \tag{3}$$

Using the above propagation of error equations and the IQE equation,

$$\eta_i = \frac{1.24}{\lambda} \cdot (\Re \pm \Delta\Re) \cdot \left(1 + \frac{\alpha_{par} \pm \Delta\alpha_{par}}{\alpha_{modal} \pm \Delta\alpha_{modal}}\right) / (1 - e^{-(\alpha_{modal} + \alpha_{par}) \cdot L}) \,, \tag{4}$$

both the average IQE and standard deviation of IQE were found. A final assumption was made that the standard deviations in the responsivity and absorption coefficients were significantly greater than the standard deviation of the fractional absorbed power. Although this was done to simplify the problem, it is also valid due to the large absorption coefficients, resulting in little change in fractional absorption with any even moderate changes in absorption.

Acknowledgments

Research carried out in part at the Center for Functional Nanomaterials, Brookhaven National Laboratory, which is supported by the U.S. Department of Energy, Office of Basic Energy Sciences, under Contract No. DE-AC02-98CH10886. The authors also acknowledge support from the Semiconductor Research Corporation Master's Scholarship and the Columbia Optics and Quantum Electronics IGERT under NSF grant DGE-1069420.

The authors would also like to acknowledge Michael W. Geis and Steven J. Spector for device fabrication and design.